World Academy of Science, Engineering and Technology
International Journal of Biomedical and Biological Engineering
Vol:6, No:6, 2012

Material density mapping on deformable 3D models of human organs

Petru Manescu[1,2], Joseph Azencot[1], Michael Beuve[2], Hamid Ladjal[1,2], Jacques Saadé[1], Jean-Michel Morreau[1],Philippe Giraud[3], Behzad Shariat[1]

Abstract—Organ motion, especially respiratory motion, is a technical challenge to radiation therapy planning and dosimetry. This motion induces displacements and deformation of the organ tissues within the irradiated region which need to be taken into account when simulating dose distribution during treatment. Finite element modeling (FEM) can provide a great insight into the mechanical behavior of the organs, since they are based on the biomechanical material properties, complex geometry of organs, and anatomical boundary conditions. In this paper we present an original approach that offers the possibility to combine image-based biomechanical models with particle transport simulations. We propose a new method to map material density information issued from CT images to deformable tetrahedral meshes. Based on the principle of mass conservation our method can correlate density variation of organ tissues with geometrical deformations during the different phases of the respiratory cycle. The first results are particularly encouraging, as local error quantification of density mapping on organ geometry and density variation with organ motion are performed to evaluate and validate our approach.

Keywords—Biomechanical simulation, Dose distribution, Image-guided radiation therapy, Organ motion, Tetrahedral mesh, 4D-CT

I. Introduction

DISPLACEMENTS and deformations of organ tissues that occur as a result of breathing can have a significant impact on radiation dosimetry for lung and liver cancer. Therefore it is very important to take into account these modifications during radiation therapy simulations in order to improve treatment planning systems. Internal details of the human body can be obtained using imaging techinques like Computer Tomography (CT) or non-invasive Magnetic Resonance Imaging (MRI). These techniques output voxelized geometries of the human body. Each voxel has a gray value which is directly related to the material density and chemical composition of the corresponding tissue [1]. These pieces of information are required to simulate the interactions between different particles used in radiation therapy (photons, protons, carbon ions) and organ tissues. The chemical composition of the tissues remains the same, but their density and position change during the breathing cycle. These changes have an important impact on the dose distribution [2] and are usually taken into account by using image registration techniques that provide non-rigid voxel mapping between datasets acquired during the breathing cycle [3], [4], [5], [6], [8]. *Heath et al.* take into account density variations by actually deforming the regular voxel grid resulting in irregular dodecahedral voxels in the dose delivery source images [7]. The drawback of this approach is that a nonrectangular deformed voxel is defined by 12 irregular boundaries that need to be detected using ray-tracing algorithms in order to calculate the energy deposited during the particle transport simulation in each voxel which is time consuming. *Velec et al* map physical dose on tetrahedral meshes in order to include organ deformations in dose distribution simulations [11], [12]. They use CT images at inhale and exhale to create two voxelized density maps at the extremes of the breathing cycle which are then used to calculate two dose distribution matrices for treatment planning. Further on, they use linear interpolation to modulate the dose distribution previously calculated from exhale position to inhale position at the centroids of each tetrahedra in the mesh. This approximation doesn't take into account density variation and assumes that dose values vary in a linear way from one position to another. The authors themselves state the fact that an ideal system for simulating dose distribution at intermediate breathing phases would require density maps for these states.

Although the geometrical models based deformable registration algorithms have been shown to accurately model the breathing motion. A realistic biomechanical model of the organ tissues may aid in understanding the effects dose distribution of tumor motion and also a response of the normal tissue in motion during treatment. Finite element modeling (FEM) can provide a great insight into the mechanics behavior of the organs and responses since finite element methods is based on the biomechanical material properties, complex organ geometry, and anatomical boundary conditions [9], [10]. The modeled object first has to be discretized into simple non-overlapping elements. This discretization allows a variety of three-dimensional element shapes, like hexahedra, tetrahedra, pyramids or prisms. Tetrahedral meshes are usually used to represent human organs because the tetrahedron is the three-dimensional simplex and any three-dimensional volume can be decomposed into tetrahedra. Human organs are not regular and their shape can be better represented with simple 3D tetrahedral elements (4 vertices) than with other type of elements. Furthermore, surface extraction algorithms usually output triangle surface meshes and it is more straightforward to create tetrahedral meshes from them. In addition, tetrahedral meshes have the greatest

[1] Université de Lyon, Université Claude Bernard Lyon 1, LIRIS, UMR 5205 F-69622, France, e-mail: firstname.name@liris.cnrs.fr
[2] Université de Lyon, Université Claude Bernard Lyon 1, IPNL, UMR 5822 F-69622, France
[3] Université Paris Descartes (Paris V), Service d'Oncologie Radiothérapie, Hôpital Européen Georges Pompidou

flexibility and are less restrictive than other mesh topologies. Another advantage of using tetrahedral elements is that, when deformed, a tetrahedra remains a tetrahedra (4 faces), whereas, as discussed before, a voxel, or hexahedral element, when deformed, turns into a dodecahedral element.

In this paper we present a new method to map material density information issued from CT images to tetrahedral meshes used for biomechanical simulations. In this way we can simulate, at the same time and within the same geometry organ motion, mass density variations and particle-matter interactions as presented in Figure 1. As opposed to the classical voxel-based geometries usually used for this kind of simulations, no additional tissue tracking or vector-field calculations are necessary.

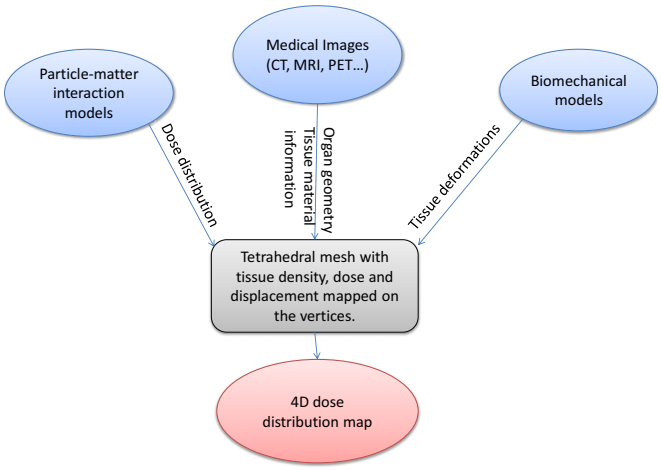

Fig. 1. General flow chart.One single structure used for both biomechanical and particle transport simulations. Details of the patient's organs are extracted from medical images and mapped on 3D deformable tetrahedral meshes used to represent human organs.

For this purpose we assign a density value to each vertex of the mesh, instead of each element in order to ensure mass density continuity. There are several reasons for doing so. First of all, organ tissues are better represented as continuous materials with variable density rather than discrete materials with constant densities. Second of all, the finite element methods use shape functions which are used to determine the value of the field variable of interest within an element by interpolating the nodal values. Furthermore, assigning density values to the vertices of the mesh representing a certain object means that we can estimate the density at any point inside the object by interpolating these values in the same way as the finite element method.

Physically-based modelling techniques like those mentioned in the introduction aim precisely at simulating the mechanical behaviour of different tissues. However, the geometrical information about organ deformation is not meaningfull for physicians. They need to study the tomographic density evolution. Hence, we propose here to construct a bridge between such biomechanical simulations and treatment planning systems: a tool to convert the deformations into dynamic CT scanner data.

This paper is structured as follows: in the next section we will briefly describe the correlation between the CT numbers and material density. Next we describe how to actually map density values to the nodes of the tetrahedral mesh by taking into account the principle of mass conservation (Section 3). In Section 4 we present a method to virtually generate CT scanner images from tetrahedral meshes to properly evaluate our density mapping algorithm (Section 5). Furthermore, this method will be used to simulate 4D-CT scanner images from deformable tetrahedral meshes. Finally we discuss the results and present possible future directions.

II. Density Mapping

We present a method of mapping material density values issued from 3D CT scanner images to the vertices of a tetrahedral mesh. Switching from a regular grid of voxels to a deformable mesh should be done by preserving the mass of the organs. That is, the total mass of a tetrahedral mesh corresponding to an organ should match the mass of the voxels representing that organ. This process is sumarized in Figure 2.

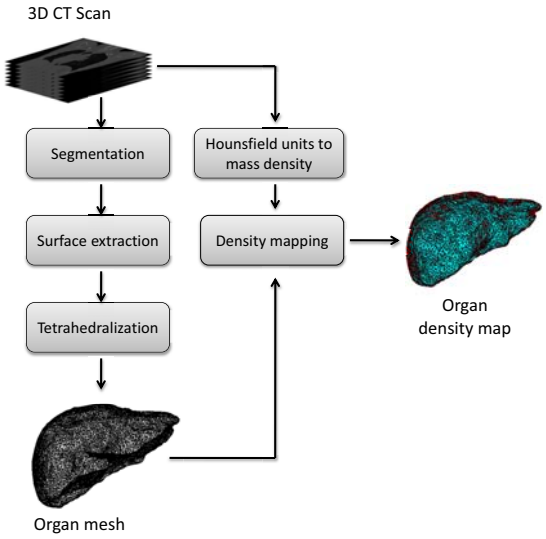

Fig. 2. 3D density mapping on a tetrahedral mesh representing a human liver

A. Hounsfield number conversion to mass density

The primary source of patient data for the present work is CT scan data. The CT image is a voxel map of linear X-ray attenuation coefficients of the different tissues to be visualized. The voxel values are scaled such that the linear X-ray attenuation coefficient of air equals -1000 and that of water equals zero. This scale is the Hounsfield scale with the unit HU.

Schneider et al. present a very precise method of converting Hounsfield values into tissue parameters (mass density and chemical composition) needed for particle-tissue interaction simulations. Their results show a linear dependence between material density and X-ray attenuation coefficients for almost all type of tissues [1].

$$\rho_M = a\rho_H + b \tag{1}$$

where ρ_M represents the mass density, ρ_H the CT intensity value in HU and a and b are constants.
This linear correlation X-ray attenuation coefficient and material density is widely assumed in the literature [13].

B. Mass of the tetrahedra

In order to calculate the density at the vertices of the mesh, we express the mass of each tetrahedron in two different ways. On one hand, it can be expressed using barycentric coordinates and linear interpolation, and on the other hand, the mass of a tetrahedron can be calculated as the sum of the volumes of intersection between the tetrahedron and the grid of voxels. We obtain thus, for every tetrahedral mesh element, one linear equation i.e we obtain a system of linear equations. Solving this system outputs the necessary values that need to be assigned to each vertex of the mesh.

Given a tetrahedron T_k with vertices A_k, B_k, C_k and D_k, its mass, $m(T_k)$ can be expressed by integrating the density value inside the tetrahedron:

$$m(T_k) = \int_{M \in T_k} \rho(M) \cdot dM \tag{2}$$

and we obtain:

$$m(T_k) = \frac{1}{4} \cdot Vol(T_k) \cdot (\rho(A_k) + \rho(B_k) + \rho(C_k) + \rho(D_k)) \tag{3}$$

where $\rho(A_k)$, $\rho(B_k)$, $\rho(C_k)$, $\rho(D_k)$ are the densities at the vertices of the tetrahedron to be determined and $Vol(T_k)$ represents the volume of tetrahedron k.
The mass of each tetrahedron in a mesh can also be written as the sum of all the intersecting voxels masses. Let $J_k = \{j, I_k^j \neq \emptyset\}$ where $\{I_k^j = V_j \cap T_k\}$ represent the intersection volume between the voxel j and the tetrahedron k (Figure 3).

$$m(T_k) = \sum_{j \in J_k} m(I_k^j) \tag{4}$$

We obtain the following equation:

$$\frac{1}{4} \cdot Vol(T_k) \cdot (\rho(A_k) + \rho(B_k) + \rho(C_k) + \rho(D_k) = \\ = \sum_{j \in J_k} Vol(I_k^j) \cdot \rho(V_j) \tag{5}$$

Equation (5) can be further rewritten:

$$\frac{1}{4} \cdot (\rho(A_k) + \rho(B_k) + \rho(C_k) + \rho(D_k) = \sum_{j \in J_k} \cdot F_k^j \cdot \rho(V_j) \tag{6}$$

where, $F_k^j = \frac{Vol(I_k^j)}{Vol(T_k)}$ is the fraction of volume occupied by each voxel inside the tetrahedron. This fractions are computed using the Monte Carlo "hit and miss" method [14] adapted

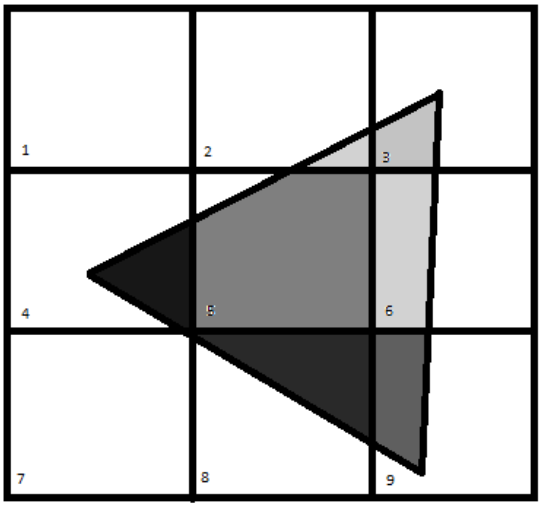

Fig. 3. Example of applying equation (4) in a 2D space: $m(T_k) = m(I_k^2) + m(I_k^3) + m(I_k^4) + m(I_k^5) + m(I_k^6) + m(I_k^8) + m(I_k^9)$

to this task. We "extract" a very large number of uniformly distributed points inside the tetrahedron. This is done by generating random barycentric coordinates as described in [15]. For every random point "extracted" we establish the voxel to which he belongs to and we count the number of points that fall in each voxel. The fractions can be approximated as follows:

$$F_k^j = \frac{N_j}{N_R} \tag{7}$$

where N_j is the number of points among the random extracted points that are inside the voxel j and N_R is the total number of random points inside the tetrahedron.

C. Density at the vertices of the mesh

For every tetrahedron k in the mesh, we write equation (5) computing the right term as described in the previous paragraph. We obtain, thus, a system of equations, in which the unknowns are the densities at the vertices of the mesh. The number of equations equals to the number of mesh elements (tetrahedra) and the number of unknowns is the number of vertices of the mesh. The system can be written as follows:

$$A \cdot X = d \tag{8}$$

where X is a vector containing the values to be determined and d is a vector containing the mean densities of each tetrahedron. A is a N_TxN_N sparse matrix in which elements a_{ij} are not equal to zero if the vertex j belongs to the tetrahedron i. Given that, the number of mesh elements is bigger than the number of mesh vertices, the system is overdetermined, i.e there is no solution that verifies every equation. However, an optimal solution can be found using the least-squares method:

$$\min_X \|A \cdot X - d\|^2 \tag{9}$$

The straightforward solution is:

$$X = (A^t \cdot A)^{-1} \cdot A^t \cdot d$$

where $(A^t \cdot A)^{-1} \cdot A^t$ is known as the pseudo-inverse matrix of A, and A^t is the transpose of the matrix A.

D. Mesh deformation

In this section we present our method to compute the vertex densities of the mesh during deformation. Let $\rho(A_k)(t)$, $\rho(B_k)(t)$, $\rho(C_k)(t)$, $\rho(D_k)(t)$ be the densities at the vertices of the tetrahedron **k** at the time step **t** with $0 \leq \mathbf{k} < \mathbf{N_T}$, where N_T is the number of tetrahedra in the mesh. We want to compute the evolution of these densities at the next time step of the deformation, i.e we want to calculate $\rho(A_k)(t+1)$, $\rho(B_k)(t+1)$, $\rho(C_k)(t+1)$, $\rho(D_k)(t+1)$ (Figure 4).

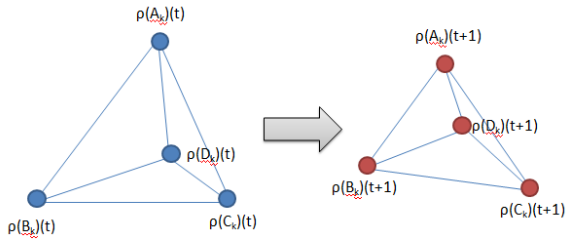

Fig. 4. Density at the vertices of a tetrahedron at instant t and $t+1$

We do so by applying the principle of matter conservation during the deformation, i.e the mass of each tetrahedron of the mesh remains constant during the deformation:

$$m(T_k)(t) = m(T_k)(t+1) \tag{10}$$

which can be written as:

$$\begin{aligned} &Vol(T_k)(t) \cdot (\rho(A_k)(t) + \rho(B_k)(t) + \rho(C_k)(t) \\ &+ \rho(D_k)(t)) = Vol(T_k)(t+1) \cdot (\rho(A_k)(t+1) \\ &+ \rho(B_k)(t+1) + \rho(C_k)(t+1) + \rho(D_k)(t+1)) \end{aligned} \tag{11}$$

So, for every tetrahedron k, we can write:

$$\begin{aligned} &\rho(A_k)(t+1) + \rho(B_k)(t+1) + \rho(C_k)(t+1) + \\ &+ \rho(D_k)(t+1) = \frac{Vol(T_k)(t)}{Vol(T_k)(t+1)} \cdot \\ &(\rho(A_k)(t) + \rho(B_k)(t) + \rho(C_k)(t) + \rho(D_k)(t)) \end{aligned} \tag{12}$$

For each time step, we build a linear system of equations as described in the previous subsection:

$$A \cdot X(t) = d(t) \tag{13}$$

III. CT Scanner Image Generation

In this section we describe a method of simulating CT density images from deformable tetrahedral meshes representing human organs. Density values have been previously assigned to the vertices of the mesh as described in Section II. This is actually the reverse procedure and we use it to evaluate our mapping algorithm by trying to reconstruct the initial scanner image. This procedure can be repeated at every step of a biomechanical simulation and thus creating a 4D CT scanner image sequence.

A. Density of a voxel

The image generation is done by assigning a corresponding density to every voxel of the image by taking into account the principle of mass preservation. Let V_j be the voxel for which we want to calculate the density, and $K_j = \{k, I_k^j \neq \emptyset\}$ be the tetrahedral elements that intersect the voxel j. The mass of the voxel j can be written as the sum of the masses of the intersection volumes between the voxel j and the tetrahedra of the mesh (Figure 5)

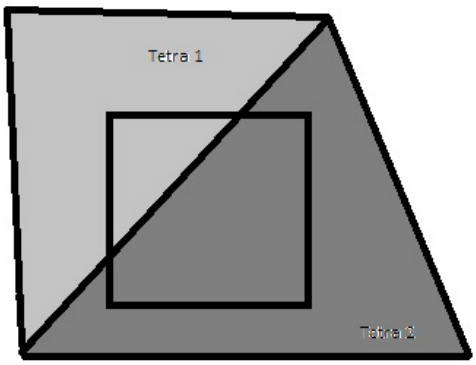

Fig. 5. 2-D example of voxel generation : $m(V_j) = m(I_1^j) + m(I_2^j)$

$$m(V_j) = \sum_{k \in K_j} m(I_k^j) \tag{14}$$

with

$$m(I_k^j) = \int_{M \in I_k^j} \rho(M) dM \tag{15}$$

IV. Evaluation

The algorithms proposed in Sections II and III have been implemented in *C++* using the *ITK* [16] and *VTK* [17] libraries. We have tested our method on several small test images as well as on two segmented images corresponding to the liver and to the left lung of a patient. The zones of interest have been segmented using the *growing region* methodology available with the *ITK-SNAP* software [18]. Surface meshes are then extracted using the *marching cubes* algorithm. We have simplified and repaired these surfaces using the *ReMesh* tool [19]. Tetrahedral meshes were generated with *TetGen* and were afterwards converted to VTK format.

A. Organ motion

We evaluated our density computation approach on liver motion due to breathing. The geometrical characteristics of the liver were obtained from experimental data (CT scan images). Breathing causes the motion and deformation of the liver. Consequently, we used two series of 3D segmented CT-scan images of a patient's liver: initial state (T_0) and final state (T_1) to generate two triangular surface meshes corresponding to the shape of the liver at two

respiratpry states. Next, we compute the displacement field between the mesh surface at T_0 to match the one at T_1 via a surface mesh registration algorithm [20] as shown in Figure 6.

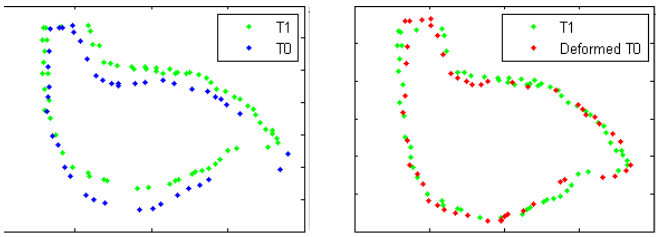

Fig. 6. Surface registration process. Coronal cut of the meshes. *Left*: Vertices of the surfaces at the two respiratory states. *Right*: Result of the mesh registration.

From the triangular surface mesh at initial state T_0, we built a tetrahedral mesh of the patient liver (Figure 7) comprising 12 514 tetrahedral elements.

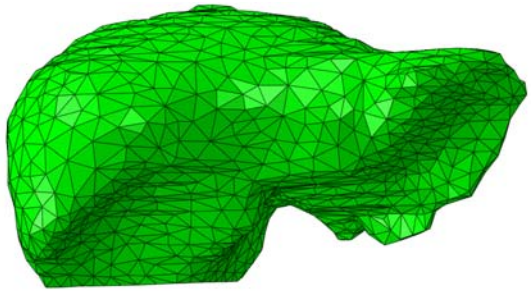

Fig. 7. Tetrahedral mesh representing the liver built with the *Abaqus* software.

To each vertex of the surface mesh we applied the displacement field previously calculated by the mesh registration algorithm as shown in Figure 8

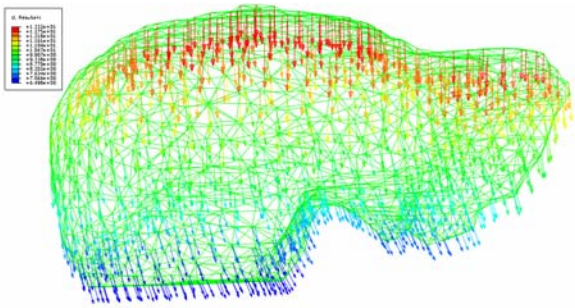

Fig. 8. Displacement field applied to the vertices of the surface of the liver mesh

The liver is supposed to have homogeneous, isotropic, elastic and compressible material properties [8]. For an isotropic elastic material the elastic energy, noted W, can be written as:

$$W(E) = \frac{\lambda}{2}\left(trE\right)^2 + \mu\, tr\left(E^2\right) \tag{16}$$

where E is the Green-Lagrange strain tensor characterizing the change in shape (or deformation) near a material point, λ and μ are the Lame's coefficients

$$E = \tfrac{1}{2}\left(grad\,U + grad^t\,U + grad^t\,U\,.\,grad\,U\right) \tag{17}$$

For small deformations, we can write the infinitesimal strain tensor :

$$\varepsilon = \frac{1}{2}(grad(U) + grad^t(U)) \tag{18}$$

These tensor are symmetric ($\varepsilon_{ij} = \varepsilon_{ji}$). The Cauchy stress tensor σ_{ij} represents internal forces acting at a material point per unit area of the deformed solid.
The relation between the stress tensor and the strain tensor is defined by Hooke's law adapted to isotropic material. For linear deformation it can be written as:

$$\varepsilon = \frac{1+\nu}{E}\sigma - \frac{\nu}{E}tr(\sigma)Id \tag{19}$$

E is Young's modulus and ν Poisson's coefficient. Other expression can be written to introduce Lame's constants.

$$\mu = \frac{E}{2(1+\nu)} \qquad \lambda = \nu\frac{E}{(1-2\nu)(1+\nu)} \tag{20}$$

where μ is Shearing coefficient and λ Compression coefficient.

The mechanical and geometrical properties of the liver structure are settled in Table I.

TABLE I
MECHANICAL PROPERTIES OF THE LIVER OBJECT [8]

Poisson's ratio	Young modulus (kPa)
0.450	7.8

The biomechanical simulation of the liver modeling was done using the *Abaqus* packages software. Further on, we compute for each vertex of the mesh its density at each time step as described in Section II and we used the method described in Section III to create a virtual CT-scan image of the liver at T_i.
Figure 9 shows our methodology of the variable density model based on the biomechanical behavior of the liver modeling.

B. Error quantification

We used several methods to evaluate our algorithms. The first one checks if the total mass of the organ does not change. We do this by comparing the mass of the voxelized object (segmented image) to the mass of the tertahedral mesh.

$$Mass(image) = \sum_{j=0}^{N_V} \rho(V_j) \cdot Vol(V_j) \tag{21}$$

where $image$ is the voxelized image of the concerned organ. The mass of the tetrahedral mesh representing the same organ can be calculated as follows:

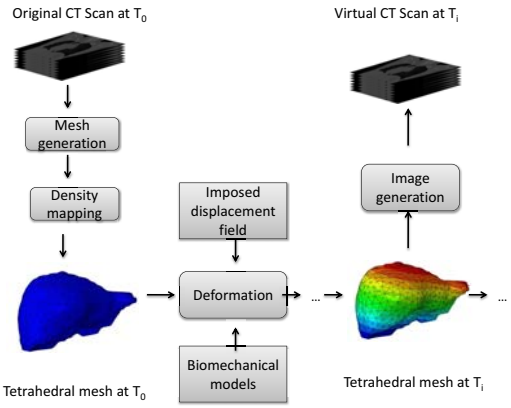

Fig. 9. Simulated 4D CT sequence generation

$$Mass(mesh) = \sum_{k=0}^{N_T} m(T_k) \tag{22}$$

where $m(T_k)$ is computed for every tetrahedron in the mesh using equation (3). The relative mass error is:

$$Error(mass)[\%] = \frac{|Mass(image) - Mass(mesh)|}{Mass(image)} \cdot 100 \tag{23}$$

Normally, if the mapping is good, the mass of the mesh should equal the mass of the initial image. This is a fair method of measuring the global error of our density mapping. However this doesn't reflect in any way the local errors that might appear when converting a discrete voxelized density distribution to a continuous tetrahedral one. For this, we use the image reconstruction method described in section 5. Let $\mathbf{I} = \{V_j, 0 \leq j < N_V\}$ be respectively the original scanner image of the object and and $\tilde{\mathbf{I}} = \{\tilde{V_j}, 0 \leq j < N_V\}$ the reconstructed image where N_V is the number of voxels be in the original image that belong to the region of interest. $\tilde{\mathbf{I}}$ and $\mathbf{I}$ should be quasi-identical, that is, we should be able to reconstruct approximately the original image. The relative mean density error can be defined as:

$$RMDE[\%] = \frac{1}{N_V} \cdot \sum_{j=0}^{N_V} e_j \tag{24}$$

with

$$e_j[\%] = \frac{|\rho(V_j) - \rho(\tilde{V_j})|}{\rho(V_j)} \cdot 100 \tag{25}$$

Ideally, the density of the reconstructed voxel $\rho(\tilde{V_j})$ should be equal to the density of the initial voxel $\rho(V_j)$. The standard deviation of the error is:

$$ESD[\%] = \sqrt{\frac{1}{N_V} \cdot \sum_{j=0}^{N_V} (e_j - RMDE)^2} \tag{26}$$

C. Results and discussion

1) Preliminary tests: We first tested our algorithms on small 3D rectangular objects. For this, we randomly cropped several test images from a CT dataset. Then, tetrahedral meshes made out of 20 tetrahedra and 18 vertices were constructed so that they cover exactly all the voxels in the test images as shown in Figure 10.

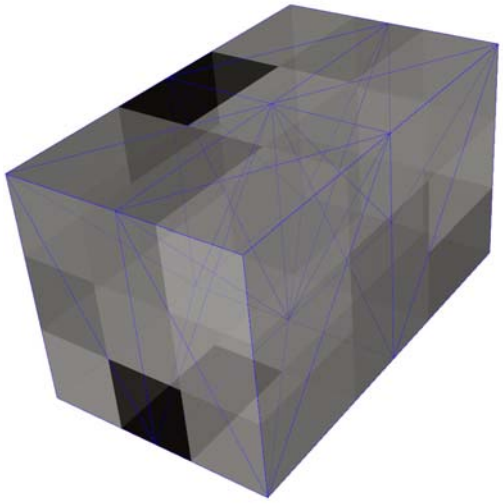

Fig. 10. A 3x3x3 voxel object croped from a CT-scan. Tetrahedralization of the voxels

We tested our algorithm on several images with sizes varying from 3x3x3 to 10x10x10 voxels. The number of elements and vertices in the tetrahedral mesh as well as the topology remained the same. We used equation (24) to evaluate the reconstruction error. The mass error for each case was insignificant (less than 1%) , which is not surprising, as the algorithm of density mapping is based on the principle of mass conservation.

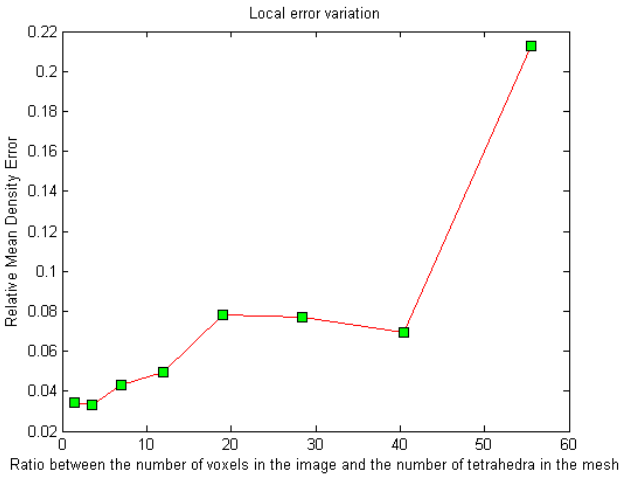

Fig. 11. Local density error variation in function of the size of the image

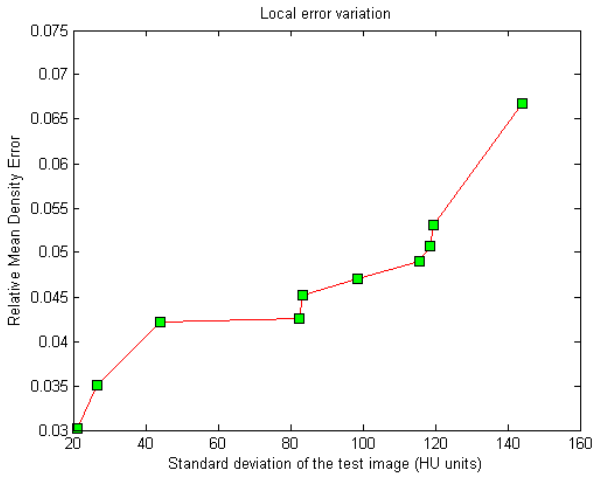

Fig. 12. Local density error variation in function of the standard deviation of the image

The mean local density error increased with the number of voxels of the image and with standard deviation of the image as shown in figures 11 and 12. This means that on one hand it became more difficult to accurately reconstruct an object as the number of vertices of the mesh got smaller compared to the number of voxels of the image and on the other hand as the heterogeneity inside that object got higher. This hypothesis was also verified by the results that follow.

2) Density mapping on organ geometry: We next tested our algorithm on segmented images representing a human liver and a lung. We first used coarse meshes (smaller number of tetrahedra), and then more refined meshes (higher number of tetrahedra). The results are shown in Table II and IV.

TABLE II
EVALUATION OF THE DENSITY MAPPING ON A LIVER GEOMETRY

No of tetra	Mass (kg)	Mass error(%)	Relative mean density error(%)	Error Standard Deviation(%)
9 643	1.348	3.7	1.7	4.4
64 768	1.351	3.5	1.2	4
90 726	1.350	3.5	0.9	3.9

TABLE III
EVALUATION OF THE DENSITY MAPPING ON A LUNG GEOMETRY

No of tetra	Mass (kg)	Mass error(%)	Relative mean density error(%)	Error Standard Deviation (%)
50 983	0.232	15	28.7	69
103 549	0.232	15	26.3	62
144 550	0.233	14.9	22.1	50

First of all, we can observe the fact that the mass of the objects were preserved with small errors. These errors were due to the fact that the meshes do not cover entirely the voxels representing the organ because their volume is usually smaller than that of the voxelized object. This was due to the simplification and smoothing previously applied to the meshes.

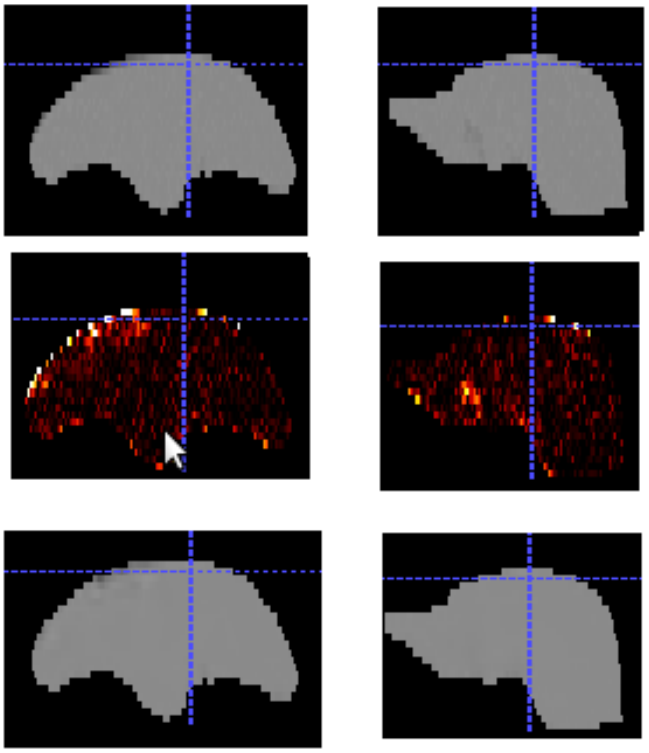

Fig. 13. Density image reconstruction of the liver. *Up*: Original segmented image - $\mathbf{I}$. *Middle*: Density error image - $|\tilde{\mathbf{I}} - \mathbf{I}|$. *Bottom* : Reconstructed image - $\tilde{\mathbf{I}}$. *Left*: Coronal view. *Right*: Sagital view. Hot color map: bright regions indicate high errors while dark regions indicate small errors

We can also notice an important difference between the relative mean density errors of the liver and that of the lung. As predicted by our initial tests, our method was able to reconstruct the liver image with minor errors (Figure 13) but the errors were more significant in the case of the lungs which is a much more heterogenous object than the liver (Figure 14). The standard deviation of the relative density error (ESD) in the case of the liver was small (4%) which indicates the fact that the error does not vary a lot from the mean relative error, which is below 2%. This can be seen in Figure 13, the local density error being uniform. In the case of the lungs, however the standard deviation of the density error is high, and as it can be seen in Figure 14, high errors occur in certain regions of the images. These regions correspond to density heterogeneities inside the lungs. We assumed that mass density is continuous, and therefore we did not take into considerations mass density discontinuities which are more present in the case of the lungs due to the presence of blood vessels and the bronchial tree. Therefore, it is more difficult to accurately reconstruct its CT-scan image.

In both cases we can observe higher errors on the border of the organs. There are two kind of errors that can occur as it can be seen in Figure 15: first, a voxel that belongs to the organ is not entirely inside the mesh (red). This is mostly because, after smoothing and simplification, the volume of

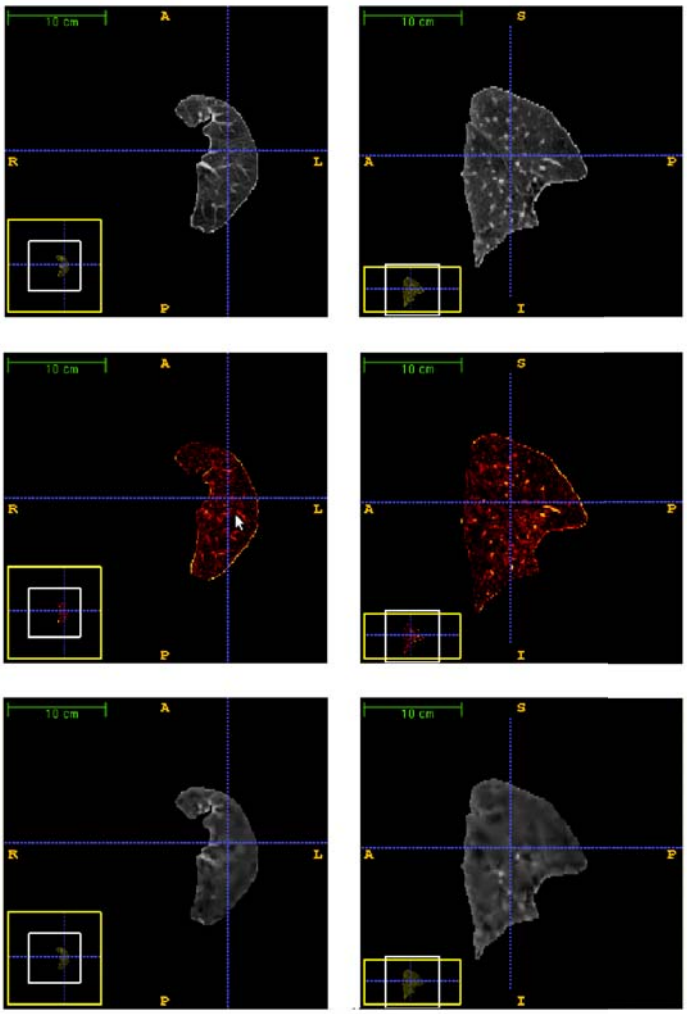

Fig. 14. Density image reconstruction of the lung. *Up*: Original segmented image - $\mathbf{I}$. *Middle*: Density error image - $|\tilde{\mathbf{I}} - \mathbf{I}|$. *Bottom* : Reconstructed image - $\tilde{\mathbf{I}}$. *Left*: Coronal view. *Right*: Sagital view. Hot color map: bright regions indicate high errors while dark regions indicate small errors

the mesh is usually smaller than the voxelized organ itself. Second, a voxel that does not belong to the organ will be reconstructed as it is inside the mesh (blue). The first type of error was reduced by extrapolating the density value calculated inside the region of the voxel that lays inside the mesh to the entire voxel. The second type of error could not be corrected. Results showed that the errors can be reduced if the number of mesh elements is increased.

3) Density variation with organ motion: In order to evaluate our density computation algorithm we compared the simulated image generated from the biomechanically deformed mesh at T_1, with the real one and we obtained the follwing results:

The mass of the mesh was preserved after deformation with an error of 2% as can be seen in table IV. However, the density error was higher in the case of the deformed mesh. Figure 16 shows the density error map. We can see that most of the errors occur in a certain zone of the liver which is due to the

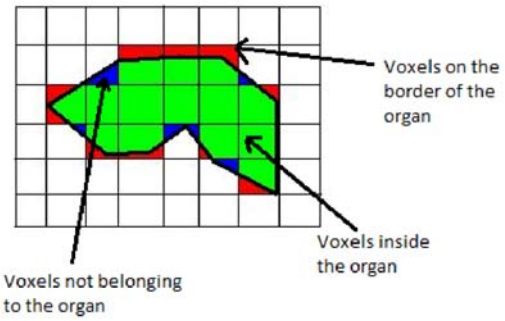

Fig. 15. Errors on the border of the organ. *Green*: voxels that belong to the segmented region and lay entirely inside the mesh. *Red*: Voxels that belong to the segmented region and are not entirely inside the mesh. *Blue*: Voxels that do not belong to the segmented region but are partially inside the mesh.

TABLE IV
EVALUATION OF THE DENSITY MAPPING ON A DEFORMING GEOMETRY

State	Mass (kg)	Mass error(%)	Relative mean density error(%)	Error Standard Deviation(%)
Initial	1.45	3.6	0.96	2.2
Deformed	1.48	5.7	7.9	30.1

surface mesh registration process that cannot properly deform the surface in that zone as it can be seen in Figure 17. We did not focus on how to improve this aspect in this study. However, in the regions where the registration was correct, our method was able to simulate accurately density voxel values.

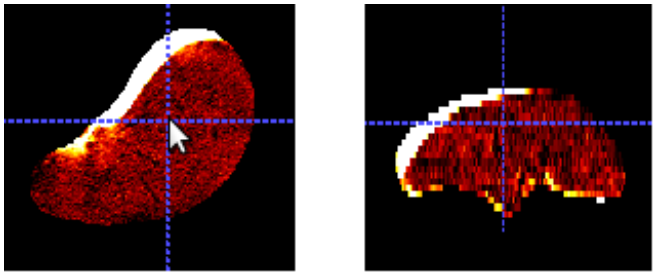

Fig. 16. Density error image $|\tilde{\mathbf{I}} - \mathbf{I}|$).*Left* : Transversal view. *Right* : Sagittal view. Hot color map: bright regions indicate high errors while dark regions indicate small errors

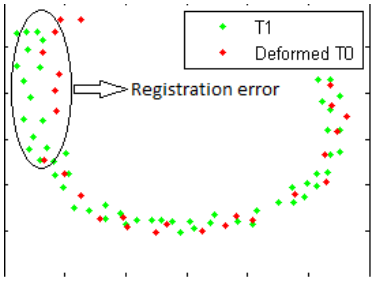

Fig. 17. Mesh registration errors. Sagittal cut of the meshes representing the liver.

V. CONCLUSIONS AND FUTURE WORKS

We have developed a novel method of representing internal details of human organs by mapping the material density acquired from the CT-scan images to the vertices of the mesh representing the objects. In order to evaluate our method we have also developed the reverse method which allows us to reproduce CT-scan images from tetrahedral meshes.

The accuracy of our mapping method depends, on one hand on the heterogeneity of the image of the object that we want to represent, and one the other hand on the number of mesh elements. For a low level of heterogeneity our method is very adapted. For regions with a large level of hetereogeneity we plan on using adaptive meshes that are refined in the heterogenous regions and coarse in the homogenous ones. Furthermore, the meshes can be refined in the regions of interest (irradiation path, tumor, organs at risk) which can significantly improve the simulation results. For this study, we assumed that the mass density is continuous inside an organ and therefore we did not take into considerations mass density discontinuities more present in the lungs due to the existance of blood vessels and bronchial tree. In the future, we plan on taking into account these discontinuities by splitting the organ mesh into regions of homogenous density.

Another important step will be to investigate in which way the density errors affect dose distribution simulations for radiation therapy. For this we plan on comparing particle-transport simulations on our simulated CT images with particle transport simulations on real CT images.

We have shown that the CT scanner image generation algorithm can be coupled with biomechanical model of the liver in order to produce a simulated sequence of a 4D-CT scanner. Consequently, with a full biomechanical model of the abdomen or thorax, intermediate voxelized density images of the patient could be generated from one respiratory state to another. These images could be included in actual treatment planning systems for liver radiation therapy. A great interest of our approach is that the simulated images could be computed with any kind of deformation models. Our approach could also be used to evaluate the quality of organ motion simulation methods. Furthermore, as mentioned before, we plan on coupling tetrahedral mesh deformations directly with particle-transport simulations producing a 4D physical dose map needed for treatment planning systems. The advantage of this approach is that no additional tissue tracking is required as oposed to the classical dose distribution calculation methods.

ACKNOWLEDGMENT

This research is supported by the ENVISION project (co-funded by the European Commission under the FP7 Collaborative Projects Grant Agreement Nr. 241851FP7), and by ETOILE's Research Program (PRRH/UCBL, under CPER 2007-13 funding).

REFERENCES

[1] W. Schneider, T. Bortfeld, W. Schelgel, *Correlation between CT numbers and tissue parameters needed for Monte Carlo simulations of clinical dose distributions*, Phys. Med. Biol. 45; 459-478, 2000.
[2] J. Seco, G. Sharp, Z. Wu, D. Gierga, F. Buettner, H. Paganetti, *Dosimetric impact of motion in free-breathing and gated lung radiotherapy: A 4D Monte Carlo study of intrafraction and interfraction effects*, Med. Phys; 35(1): 356-366, 2008.
[3] M. Rosu, I.J. Chetty, J.M. Balter, M.L. Kessler, D.L. McShan, R.K. Ten Haken *Dose reconstruction in deforming lung anatomy: dose grid size effects and clinical implications*. Med. Phys;32:248795, 2005.
[4] D. Sarrut, *Deformable registration for image-guided radiation therapy*, Zeitschrift fur medizinische Physik 16 (4), 285-97, 2006.
[5] V. Boldea, G. Sharp, S. Jiang, D. Sarrut, *4D-CT lung motion estimation with deformable registration. Quantification of motion nonlinearity and hysteresis*, Medical Physics 35 (3), 1008, 2008.
[6] S. Flampouri, S.B. Jiang, G.C. Sharp, J. Wolfgang, A.A. Patel, N.C. Choi, *Estimation of the delivered patient dose in lung IMRT treatment based on deformable registration of 4D-CT data and Monte Carlo simulations.* Phys. Med. Biol;51:276379, 2006.
[7] E. Heath, J. Sentjens. *A direct voxel tracking method for four-dimensional Monte Carlo dose calculation in deforming anatomy.* Med. Phys;33:43445, 2006.

[8] M. Velec, J. Moseley, B. Math, C. Eccles, T. Craig, M. Sharpe, L. Dawson, K. Brock, *Effect of breathing motion on radiotherapy dose accumulation in the abdomen using deformable registration*. Int. J Radiation Oncology Biol. Phys., Vol 80, No. 1, 265-272, 2011.

[9] J. Saade, A.L. Didier, P.F. Villard, R. Buttin, J.M. Moreau, M. Beuve, B. Shariat, *A preliminary study for biomechanical model of the respiratpry system*, VISAPP, 2010.

[10] A. Al-Mayah , J. Moseley , M. Velec, K. Brock , *Toward efficient biomechanical-based deformable image registration of lungs for image-guided radiotherapy*, Phys. Med. Biol. volume 56, number 15, 56 4701, 2011.

[11] M. Velec, J. Moseley, B. Math, T. Craig, , L. Dawson, K. Brock, *Accumulated dose in liver stereotactic body radiotherapy:positioning, breathing and deformation effects*. Int. J Radiation Oncology Biol. Phys., Vol 80, No. 1, 1-9, 2011.

[12] K. Brock , D. McShan , R. Ten Haken , S. Hollister , L. Dawson , J. Balter , *Inclusion of organ deformation in dose calculations*, Medical Physics , Vol. 30 (3), 290-295, 2003.

[13] A. Bhatt , R. Wakhedhar , *Reverse Engineering of Human Body: A B-spline based Heterogeneous Modeling Approach*, Computer-Aided Design and Applications, www.cadanda.com, 2008.

[14] M. Kalos , P. Whitlock , *Monte Carlo Methods*, Wiley, New York, 1986.

[15] C. Rocchini , P. Cignoni , *Generating random points in a tetrahedron*, Journal of Graphics Tools, Vol. 5, 200, 2001.

[16] T. Yoo , MJ. Ackerman , WE. Lorensen , *Engineering and algorithm design for an image processing Api: a techiincal report on ITK - the Insight Toolkit*, Stud Health Technol Inform 85: 586-92, http://www.itk.org, 2002.

[17] W. Schroeder , K. Martin , B. Lorensen , *The Visualization Toolkit*, ISBN 978-1930934191, http://www.vtk.org, 2006.

[18] P. Yushkevich , J. Piven , H. Hazlett , R. Smith , S. Ho , J. Gee , G. Gerig , *User-guided 3D active contour segmentation of anatomical structures: Significantly improved efficiency and reliability*, Neuroimage 31(3);1116-28, 2006.

[19] M. Attene , B. Falcidieno , *ReMesh: An interactive Environment to Edit and Repair Triangle Meshes*, Procs of Shape Modeling International (SMI '06), IEEE C.S Press; 271-276, 2006.

[20] Z. Zhang , *Iterative Point Matching for Registration of Free-form Curves*, International Journal of Computer Vision, 13:2, 119-152, 1994.